Chalcogenide Letters

Tech Science Press

http://doi.org/10.32604/cl.2026.083065

ARTICLE

Effect of PbO_2 and Bi_2O_3 on the Physical, Optical, and Gamma-Ray Shielding Properties of Boro-Tellurite Glasses

Aljawhara H. Almuqrin[1], Manjunatha[2], M. I. Sayyed[3,4,5,*], Ashok Kumar[6,7,*] and A. S. Bennal[8]

[1]Department of Physics, College of Science, Princess Nourah Bint Abdulrahman University, P.O. Box 84428, Riyadh, 11671, Saudi Arabia
[2]Department of Physics, School of Engineering and Technology, CMR University, Bengaluru, India
[3]Department of Physics, Faculty of Science, Isra University, Amman, Jordan
[4]Department of Physics, Dogus University, Dudullu-Ümraniye, Istanbul, Türkiye
[5]Department of Physics and Technical Sciences, Western Caspian University, Baku, Azerbaijan
[6]Department of Physics, University College, Benra, Dhuri, India
[7]Department of Physics, Punjabi University, Patiala, India
[8]Department of Studies in Physics, Karnatak University, Dharwad, India
*Corresponding Authors: M. I. Sayyed. Email: dr.mabualssayed@gmail.com; Ashok Kumar. Email: ajindal9999@gmail.com

Received: 28 March 2026; Accepted: 08 June 2026; Published: 02 July 2026

ABSTRACT: The human exposure to hazardous ionizing radiation is increased due to the progression of nuclear technology across energy, medicine, and industrial sectors, etc. Developing transparent shielding materials is essential to overcome the structural and opacity limitations of traditional materials like concrete. The $30TeO_2$-$xPbO_2$-xBi_2O_3-$(70 - 2x)B_2O_3$ (x = 10, 12, 14 and 16 mol%) glasses are prepared via the melt-quenching technique. The density (ρ) increases from 4.759 to 5.561 g cm^{-3} due to the incorporation of heavy metal oxides (HMOs). The molar volume (V_m) increases from 32.194 to 33.657 cm^3 mol^{-1}. The oxygen packing density (OPD) decreased from 80.761 to 75.468. It is due to the depolymerization and the formation of Non-Bridging Oxygens (NBOs). The calculations based on the Makishima-Mackenzie model showed a consistent reduction in elastic moduli. The optical band gap energy (E_g) decreases from 2.969 to 2.813 eV. The substitution of B_2O_3 with PbO_2 and Bi_2O_3 greatly enhances photon attenuation. The radiation shielding evaluations using Phy-X software confirmed that the mass attenuation coefficient (MAC) reached as high as 72.00 cm^2 g^{-1} at 0.015 MeV. This high-density PbBi16 sample provided the most compact shielding as indicated by the lowest half-value layer (HVL) of 0.0293 cm and a reduced mean free path (MFP).

KEYWORDS: Borotellurite glasses; gamma-ray shielding; optical properties; Makishima-Mackenzie model; HMO

1 Introduction

The development of nuclear technology in energy production, medicine, the food irradiation industry and academic scientific research has made people more exposed to ionising or nuclear radiation [1,2]. Gamma radiation (γ) is regularly useful in some ways, but it is also very hazardous to living things as well as the environment. In living things, these radiations can pass through easily and cause serious health effects by damaging cells and molecules [3]. Due to this, developing effective radiation shielding targets or materials has become an important scientific and technological challenge in modern material science [4].

Concrete is widely used due to its very dense nature and can block γ rays efficiently [5]. But these common resources have a lot of problems. Concrete needs to be very thick to work as a shield, and it often is not clear and flexible in terms of structure [6]. These restrictions have led researchers to investigate other target materials that provide effective radiation shielding and are also stronger and safer for the environment.

Several researchers, including our group, show that HMO glasses have become auspicious materials for radiation shielding applications in recent decades [7–10]. Related to other shielding materials as mentioned above, glass has a series of benefits. These include ease of fabrication, structural homogeneity, optical transparency, adjustable composition and the ability to hold some amounts of different HMOs in a single composite [11]. It is possible to make effective glass materials that can be useful in nuclear radiation technologies.

Tellurite (Te) based glasses have gotten a lot of consideration due to their unique physical and structural features compared to other types of glass materials [12]. Also, it is well known for its high density, higher refractive index, great optical features, and absorption of nuclear radiation than other glass-forming systems such as silicate or borate glasses [13]. Pure Te glasses have some good features, but they often don't last long in terms of chemical and mechanical stability. To address these constraints and further improve their nuclear radiation shielding efficacy, the incorporation of additional HMOs has been broadly investigated and reported [14]. Among them, lead oxide (PbO) and bismuth oxide (Bi_2O_3) are effective modifiers that have been studied for radiation shielding [15,16]. These two compounds are very interesting because they have high atomic numbers and atomic masses. The study on borate glasses containing cadmium and copper explored how potassium fluoride influences their physical and structural features [17]. The investigations into chromium-activated tellurite-borate glasses have demonstrated their high efficiency and stability for use in LED technology [18]. The nanocomposite films using copper bismuth oxide have been investigated for their ability to block radiation and their internal structural features [19]. The impact of Bi_2O_3 on the behaviour of phosphate-based glasses has been evaluated to improve their shielding performance [20].

Borate (B_2O_3) based glasses are also well studied because they can easily be made into glass, are very stable at high temperatures and can hold various modifying oxides. B_2O_3 forms a solid glass network out of BO_4 and BO_3 structural units [21]. Further, these glasses can have low melting points and good chemical stability, which makes them good hosts for glass systems that can do more than one thing [22].

A good way to make advanced radiation shielding materials that work better is to mix tellurite and borate glass networks with HMOs. This study deals with B_2O_3-TeO_2-based glass composites with varying PbO and Bi_2O_3. Incorporating these parts in a systematic way figures out how composition, density, optical properties and radiation attenuation efficiency are related. This study's results are projected to support the advancement of classy glass materials with improved shielding properties. Furthermore, this study presents potential uses in nuclear power plants, radioactive waste storage, etc.

2 Materials and Methods

2.1 Glass Synthesis

TeO_2-PbO_2-Bi_2O_3-B_2O_3 glasses were prepared via. melt-quenching technique. The TeO_2, PbO_2, Bi_2O_3, and B_2O_3 oxides were weighed, and a batch of 15 g was prepared. The oxides were then ground together in an agate mortar for 30 min. The mixture was transferred to an alumina crucible. The batch was melted at 1000°C for 20 min. The molten mixture was quickly poured onto a pre-heated brass plate. To prevent cracking due to thermal stress, the glass discs were annealed for 2 h, then allowed to cool slowly. The photo of the samples is shown in Fig. 1.

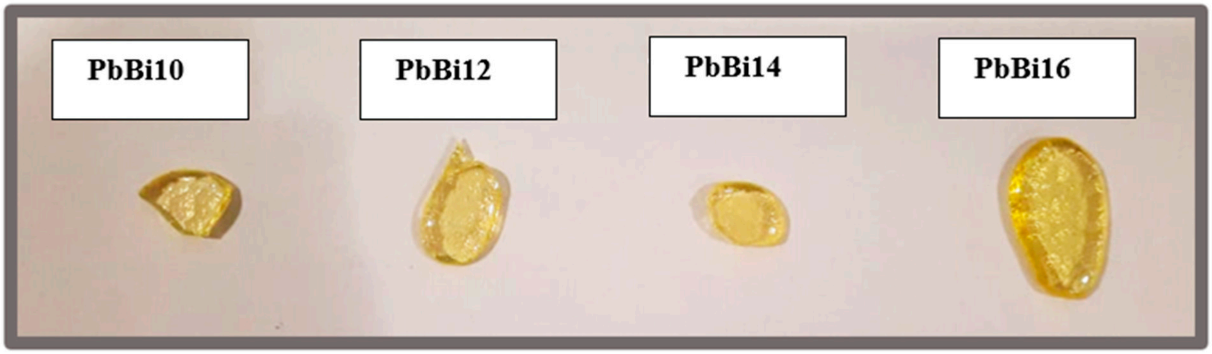

Figure 1: Picture of the samples.

The density was measured using the Archimedes method as [23–25]:

$$\rho = \frac{weight\ of\ the\ glass\ in\ air}{weight\ of\ the\ glass\ in\ air - weight\ of\ the\ glass\ in\ water}\ \mathrm{g\cdot cm^{-3}} \tag{1}$$

The chemical composition and density are listed in Table 1. The physical parameters are calculated using the standard formulae described in previous works and are provided in Table S1 of the supplementary information [26–28].

Table 1: Chemical composition and density of the glasses.

Glass Code	Mol% of the Components Present in the Glass				Wt. Fraction of the Elements Present in the Glass					Density g cm^{-3}
	B_2O_3	TeO_2	Bi_2O_3	PbO_2	B	O	Te	Bi	Pb	
PbBi10	50	30	10	10	0.0706	0.2715	0.2499	0.2728	0.1352	4.759
PbBi12	46	30	12	12	0.0605	0.2509	0.2327	0.3049	0.1511	5.026
PbBi14	42	30	14	14	0.0516	0.2329	0.2177	0.3328	0.1650	5.293
PbBi16	38	30	16	16	0.0439	0.2171	0.2045	0.3573	0.1771	5.561

2.2 Mechanical Analysis

The elastic moduli were calculated using the Makishima-Mackenzie model [29–31]. The calculations involve the total atomic packing density (V_t) and the dissociation energy (G_t) as two input parameters:

$$V_t = \left(\frac{1}{V_m}\right)\sum V_i x_i \tag{2}$$

$$G_t = \sum G_i x_i \tag{3}$$

In these equations, x_i is the mole fraction, and V_i is the packing density factor of the i-th oxide component.

The elastic moduli are determined as [26–28]:

Young's modulus (E):

$$E = 8.36 V_t G_t \tag{4}$$

Bulk modulus (B):

$$B = 10V_t^2 G_t \quad (5)$$

Shear modulus (G):

$$G = \frac{30V_t^2 G_t}{(10.2V_t - 1)} \quad (6)$$

Longitudinal modulus (L):

$$L = K + \left(\frac{4}{3}\right) \quad (7)$$

2.3 Optical Analysis

The absorption spectra were recorded using a PerkinElmer Lambda 19 UV-Vis spectrophotometer from 190–1000 nm. The E_g has been estimated using Tauc's plot method. This method relates the absorption coefficient (α) and photon energy ($h\nu$) as [32,33]:

$$(\alpha h\nu)^{1/2} = \mathrm{B}\left(h\nu - E_g\right) \quad (8)$$

The quantity $(\alpha h\nu)^{1/2}$ is plotted against $h\nu$. The linear portion of this curve is then extrapolated to the x-axis where absorption is zero. The intercept provides the value of E_g. The E_g was utilized to calculate additional optical parameters and is shown in Table S2 of the supplementary information.

Optical electronegativity (χ^*):

$$\chi^* = 2.688\ \mathrm{E_g} \quad (9)$$

Linear dielectric susceptibility ($\chi^{(1)}$):

$$\chi^{(1)} = (\mathrm{n}^2 - 1)/4\pi \quad (10)$$

Third-order nonlinear optical susceptibility (χ^3):

$$\chi^3 = \mathrm{A}/(4\,\pi)^4\,(\mathrm{n} - 1)^4 \quad (11)$$

Nonlinear refractive index ($\mathbf{n_2}^{\mathbf{optical}}$):

$$\mathbf{n_2}^{\mathbf{optical}} = 12\,\pi\,\chi^3/\mathrm{n} \quad (12)$$

2.4 Gamma Ray Shielding Evaluation

The linear attenuation coefficient (LAC) is obtained as:

$$I_t = I_0 e^{-LAC.t} \quad (13)$$

I_0 and I_t are the incident and transmitted intensity of photons through a material of thickness t.

The MAC can be obtained as:

$$MAC = \frac{LAC}{\rho} \quad (14)$$

The *HVL* and *MFP* are obtained as:

$$HVL = \frac{ln(2)}{LAC} \quad (15)$$

$$MFP = \frac{l}{LAC} \quad (16)$$

The Phy-X software enables the accurate calculation of the MAC directly from a material's chemical composition across various energy levels [34]. It automates the derivation of secondary shielding metrics, including the *LAC*, *HVL* and *MFP*. By replacing time-consuming manual calculations, Phy-X/PSD provides an efficient and reliable platform for the theoretical screening, comparison, and design of novel shielding products prior to physical fabrication. The obtained data is presented in Tables S3–S6 of the supplementary information.

3 Results and Discussion

3.1 Physical and Structural Parameters

The ρ increases from 4.759 (PbBi10) to 5.561 g cm^{-3} (PbBi16) as shown in Fig. 2. The lighter B_2O_3 (69.62 g mol^{-1}) is being progressively replaced by the much heavier HMOs, PbO_2 (239.2 g mol^{-1}) and Bi_2O_3 (465.9 g mol^{-1}) [35,36]. This also results in an overall rise in the mass of the glass matrix sharply with doping. The average molar mass (M_m) of the glass composition rises from 153.211 to 187.165 g mol^{-1}. The V_m increases from 32.194 to 33.657 cm^3 mol^{-1} (Fig. 2). This implies that the rate of volume expansion exceeds the rate of mass accumulation [35,36]. The addition of Pb^{4+} and Bi^{3+} ions expands the glass network, increasing the free volume (Fig. 2). The concentration of dopant metal ions (N) increases from 1.871 to 2.863×10^{21} ions cm^{-3}. As the mole percentage of PbO_2 and Bi_2O_3 increases, the N naturally rises. The separation between boron atoms ($d_{B\text{-}B}$) decreases from 3.767 to 3.559×10^{-8} cm. As the content of B_2O_3 is reduced from 50 to 38 mol%, the boron structural units rearrange into smaller domains as shown in Fig. 3. This results in a slight reduction in the average inter-atomic distance between boron centers. The r_i decreases from 8.116 to 7.042×10^{-8} cm. The polaron radius (r_p) decreases from 3.270 to 2.838×10^{-8} cm. The ions come closer with increasing metal-ion number density, as shown in Fig. 3. This enhances the localisation of charge carriers, as indicated by the shrinking polaron radius [37]. The field strength (F) increases from 1.870 to 2.484×10^{15} cm^2. The reduction in r_i leads to a stronger local electric field. It influences the polarization of the surrounding oxygen ions. The OPD decreases from 80.761 to 75.468 as shown in Fig. 4. A lower OPD signifies a loosely packed structure. The addition of HMOs breaks the continuous B-O-B linkages. It results in the formation of NBOs and the disruption of the rigid network. The OMV increases from 12.382 to 13.251 cm^3 mol^{-1} as shown in Fig. 4. It confirms the increase in volume available per mole of oxygen. The elastic moduli decrease with the addition of PbO_2 and Bi_2O_3, as shown in Fig. 5. The mechanical stiffness reduces as the formation of NBOs disrupts the network. It is due to the replacement of stronger B-O bonds by weaker Pb-O and Bi-O bonds. The decrease in OPD also creates voids. It makes the material more susceptible to deformation under stress.

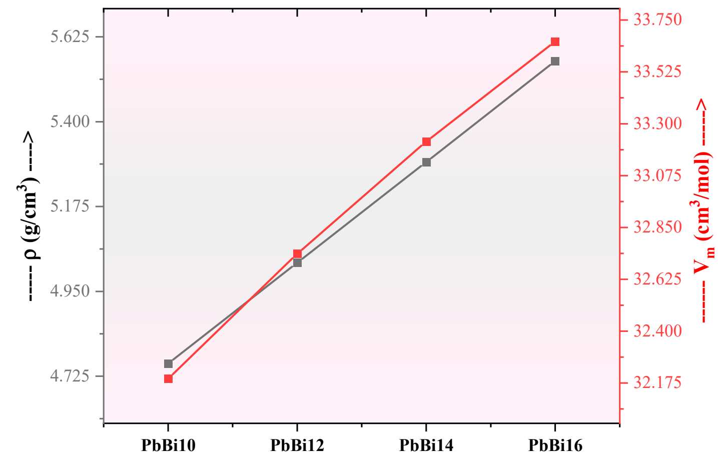

Figure 2: Variation of ρ and V_m for the present samples.

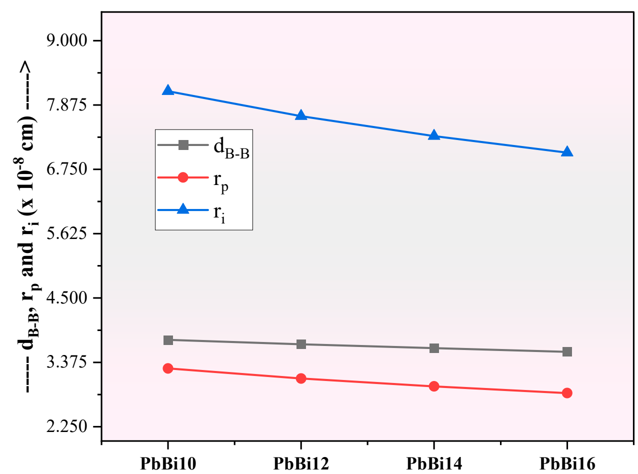

Figure 3: Variation of $d_{B\text{-}B}$, r_i and r_p for the present samples.

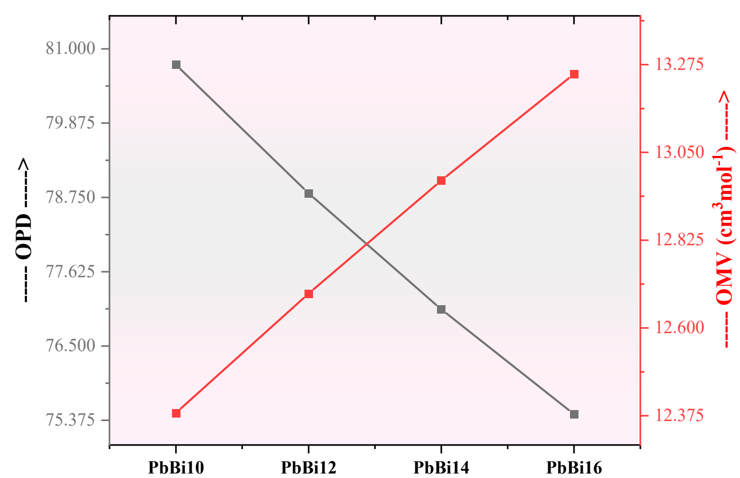

Figure 4: Variation of OPD and OMV for the present samples.

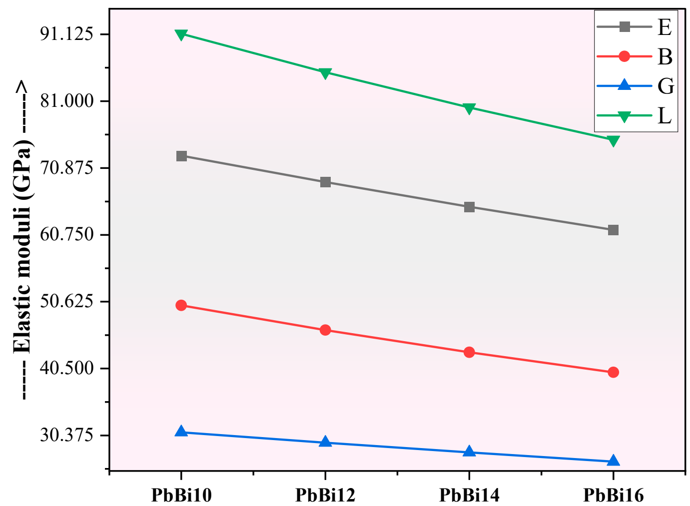

Figure 5: Variation of elastic moduli for the present samples.

3.2 Optical Properties

The Tauc's plot is shown in Fig. 6. The E_g decreases from 2.969 eV to 2.813 eV as shown in Fig. 7. It is a direct consequence of structural depolymerization. The formation of NBOs creates localized defect states at the top of the valence band. The electrons in NBOs are less tightly bound than those in bridging oxygens. The energy required for an electronic transition is reduced. The n increases from 2.405 to 2.449 as shown in Fig. 7. This is due to the high concentration of HMOs. Pb^{4+} and Bi^{3+} are highly polarizable cations with larger ionic radii. It increases the electron density and polarizability resulting in a stronger interaction with incident light. The dielectric constant (ε) increases from 5.786 to 5.999. The optical dielectric constant (ε_{opt}) increases from 4.786 to 4.999. Since the dielectric behavior follows the refractive index trend. The R_m and α_m increase from 19.789 to 21.035 cm^3 mol^{-1} and 7.849 to 8.343 × 10^{-24} cm^3. The increase in R_m and α_m confirms the electronic softening of the glass. The electron clouds surrounding the oxygen and HMOs become more deformable due to formation of NBOs. The electronic polarizability (α_e) increases from 8.726 to 8.871 × 10^{23}. It is due to the specific contribution of electronic displacements to the total polarizability, further supporting the increase in the refractive index. The reflection loss (R_L) and transmission (T) increases from 0.170 to 0.177 and decrease from 0.709 to 0.699, respectively, as shown in Fig. 8. The reflection at the air-glass interface becomes more significant with a rise in refractive index. It leads to higher reflection losses and a reduction in optical transmission. The Metallization (M) decreases from 0.385 to 0.375. A less than 1 value of M indicates that the glasses are insulators. The decrease in M indicates a shift towards semi-conducting behavior [35,36]. The decrease in E_g increases the metallic character. The χ^* decreases from 0.798 to 0.756. This parameter quantifies the ability of the anion matrix to hold valence electrons. It indicates that the electrons are less tightly held in the high-Pb/Bi glasses compared to the base glass. It is consistent with the formation of loosely bound NBOs. The $\chi^{(1)}$ increases from 0.381 to 0.398. This linear optical parameter is directly derived from the refractive index and confirms the material's increasing linear response to an optical field. The χ^3 decreases from 1.751 to 1.548 × 10^{-15} esu. The $\mathbf{n_2}^{\mathbf{optical}}$ decreases from 2.742 to 2.382 × 10^{-14} esu. It is due to the structural constraints imposed by the higher field strength (F) and reduced inter-nuclear distances, which may dampen the anharmonic motion of the electrons required for non-linear effects [37].

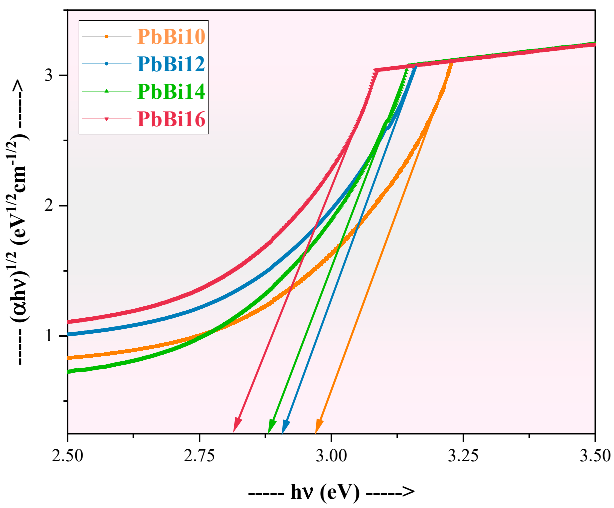

Figure 6: Tauc's plot for the present samples.

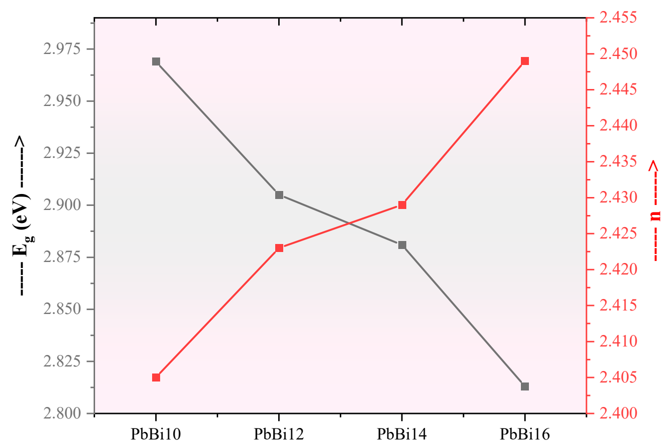

Figure 7: Variation of E_g and n for the present samples.

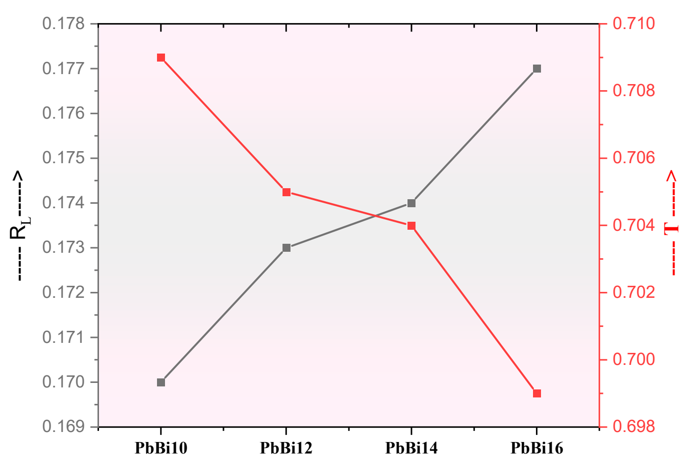

Figure 8: Variation of R_L and T for the present samples.

3.3 Gamma Ray Shielding Properties

The MAC of the TeO_2–Bi_2O_3-PbO_2-B_2O_3 glass systems was computed utilizing Phy-X software. The energy interval (in MeV) employed in this investigation was $0.015 \leq E \leq 15$. Fig. 9 depicts the MAC pattern of the TeO_2–Bi_2O_3-PbO_2-B_2O_3 glass systems. The MAC for all samples diminished as energy rose. The discontinuities in MAC at 0.04 and 0.1 MeV are due to the K-shell energy of heavy metals like Te, Pb, and Bi. The principles in radiation physics indicate that photons interact with a glass through three principal mechanisms. The initial phenomenon is termed the photoelectric effect (PE), illustrated in Fig. 9 for energy less than 0.8 MeV. It exerts significant effects on low-energy photons. For PbBi10 at 0.015 MeV, the MAC (in cm^2/g) was 59.94, but diminished to 3.93 at 0.06 MeV. Identical behavior was noted in the PbBi12, PbBi14 and PbBi16 samples within this energy range. The second phenomenon, termed Compton scattering (CS), exhibits a cross section that is largely independent of elemental composition. As illustrated in Fig. 9, all samples within the range of 0.8 to 4 MeV exhibited roughly comparable MAC values. As an illustration, for PbBi10 and PbBi12 at 2 MeV, the MAC was 0.0439 and 0.0441 cm^2/g, respectively. Pair production (PP) is the most crucial component for high photon energy region. The probability of occurrence of this phenomenon is proportional to Z^2. The MAC at the last few energies grew gradually up to 15 MeV, the maximum energy used in this investigation, as shown in Fig. 9. The findings of the attenuation graph showed that MAC rose when the concentrations of PbO_2 and Bi_2O_3 varied between 10 and 16 mol%. The sample containing the highest concentrations of PbO_2 and Bi_2O_3 (PbBi16) exhibited the greatest attenuation factor, while conversely, the sample with the lowest concentrations showed the least.

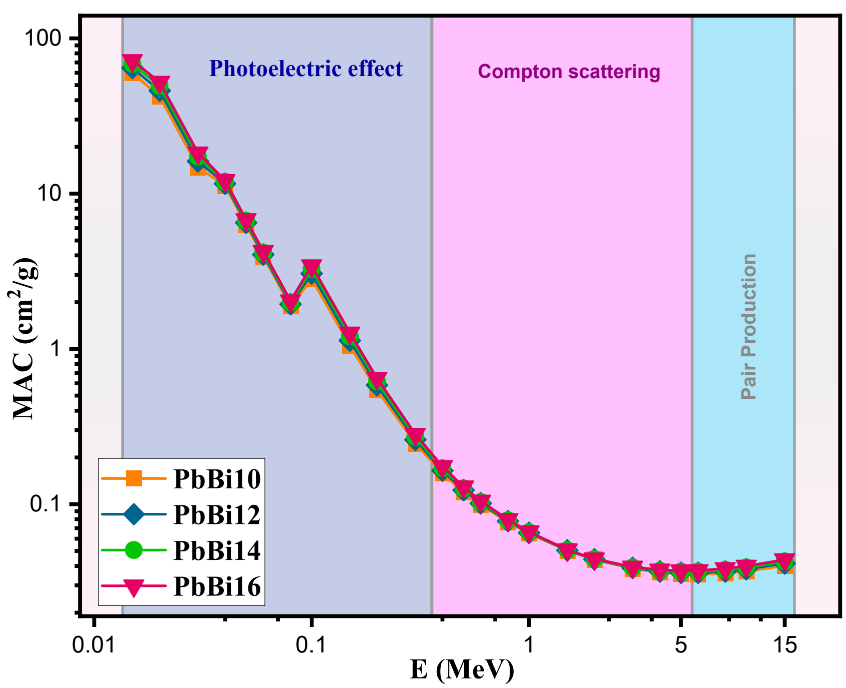

Figure 9: The MAC of the TeO_2-Bi_2O_3-PbO_2-B_2O_3 glasses.

The LAC value, as seen in Fig. 10, was variable with energy and typically diminished sharply as the energy rose from 15 keV to 6 MeV. The glass reduces the intensity of low energy photons, preventing most from penetrating it. With increasing energy, the photons traversed the sample easily, indicating that the LAC was comparatively low for high-energy photons. As an illustration, for PbBi10 at 0.15 and 8 MeV, the

LAC values were 4.99 and 0.171 cm^{-1}, respectively. The high-density material offers superior shielding compared to low-density glass. The PbBi16 sample possesses the greatest LAC values across all energy levels. PbBi10 exhibited the lowest density and the lowest LAC. Consequently, PbBi16 offers superior shielding owing to enhanced contacts compared to the PbBi10, PbBi12 and PbBi14 samples.

Two further parameters commonly employed to describe photon attenuation are the HVL and MFP. A reduced HVL and MFP are advantageous as they require a smaller space to attenuate an equivalent quantity of photons. The HVL of the TeO_2-Bi_2O_3-PbO_2-B_2O_3 glass systems is plotted in Fig. 11. It illustrates that PbBi16 exhibited the lowest HVL and optimal attenuation, attributable to the elevated weight fractions of Bi_2O_3 and PbO_2, as well as its comparatively high density. Conversely, the PbBi10, which had the lowest density and the least quantity of Bi_2O_3 and PbO_2, showed the worst attenuation. The HVL decreased with a rise in energy, leading to better attenuation against gamma rays. Additionally, Fig. 11 shows that the HVL increased with increasing energy. This implies that low-energy photons can be adequately shielded by a thin layer, but high-energy photons require a thicker layer. The HVL of the PbBi10–PbBi16 glasses at 0.06 MeV was 0.0371, 0.0341, 0.0315 and 0.0293 cm, whereas at 10 MeV, the values increased to 3.94, 3.62, 3.35 and 3.12 cm, respectively.

The MFP of the TeO_2-Bi_2O_3-PbO_2-B_2O_3 glasses is represented graphically in Fig. 12. The MFP for all glasses exhibited a quick increase up to 0.08 MeV with rising energy, followed by a slowing in the rate of growth. The reduction in MFP was attributed to the increased PbO_2 and Bi_2O_3 levels. A comparison of the MFP values of PbBi10 and PbBi16 revealed that PbBi10 needed a greater MFP than PbBi16. The MFP ratio between PbBi10 and PbBi16 was 1.41 at 0.1 MeV, 1.34 at 0.3 MeV, 1.23 at 0.6 MeV and 1.18 at 2 MeV. This signifies that the MFP ratio between PbBi10 and PbBi16 was comparatively elevated at lower energy, indicating that PbO_2 and Bi_2O_3 influenced the MFP, resulting in enhanced shielding efficiency at lower energies.

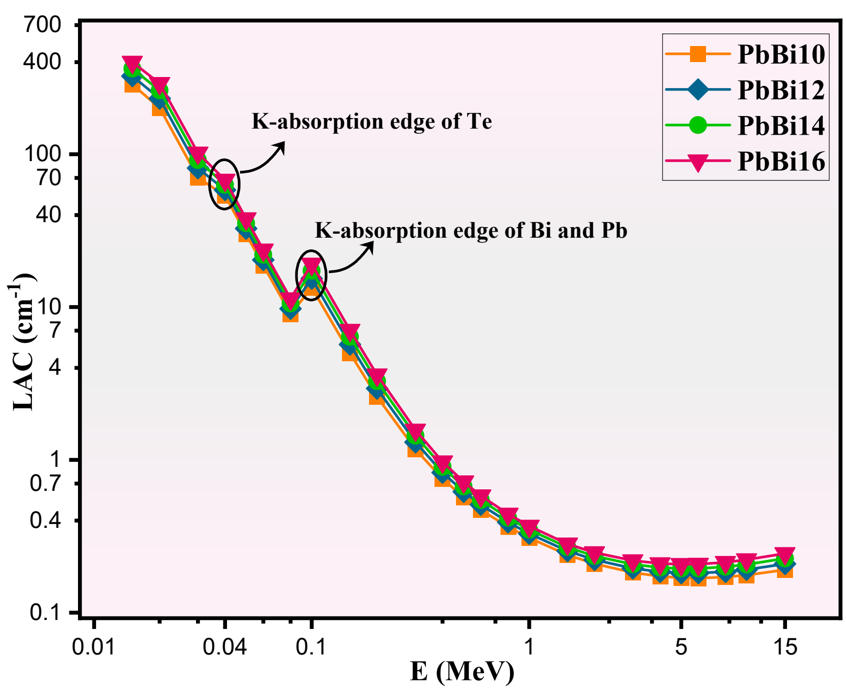

Figure 10: The LAC of the TeO_2-Bi_2O_3-PbO_2-B_2O_3 glasses.

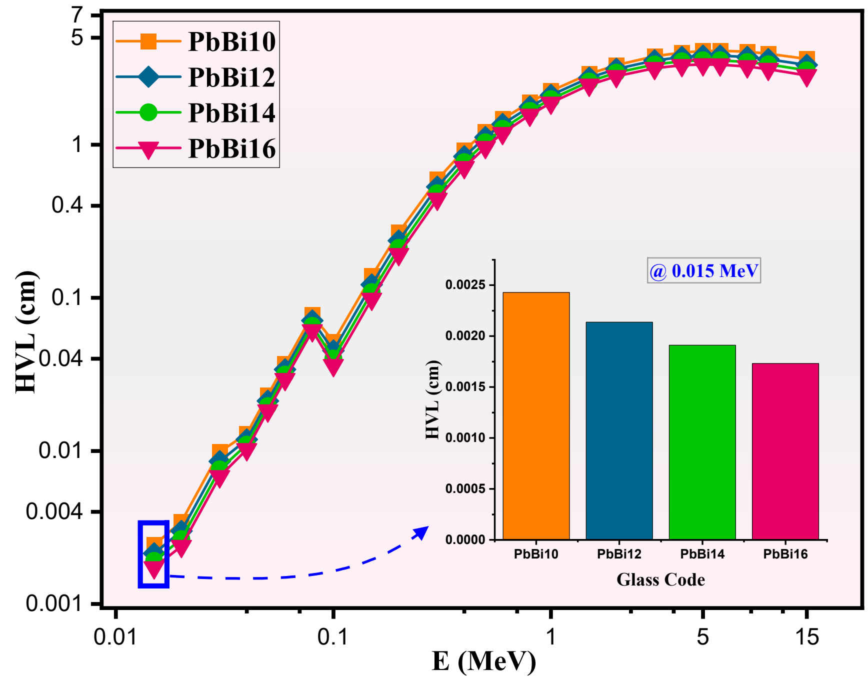

Figure 11: The HVL of the TeO_2-Bi_2O_3-PbO_2-B_2O_3 glasses.

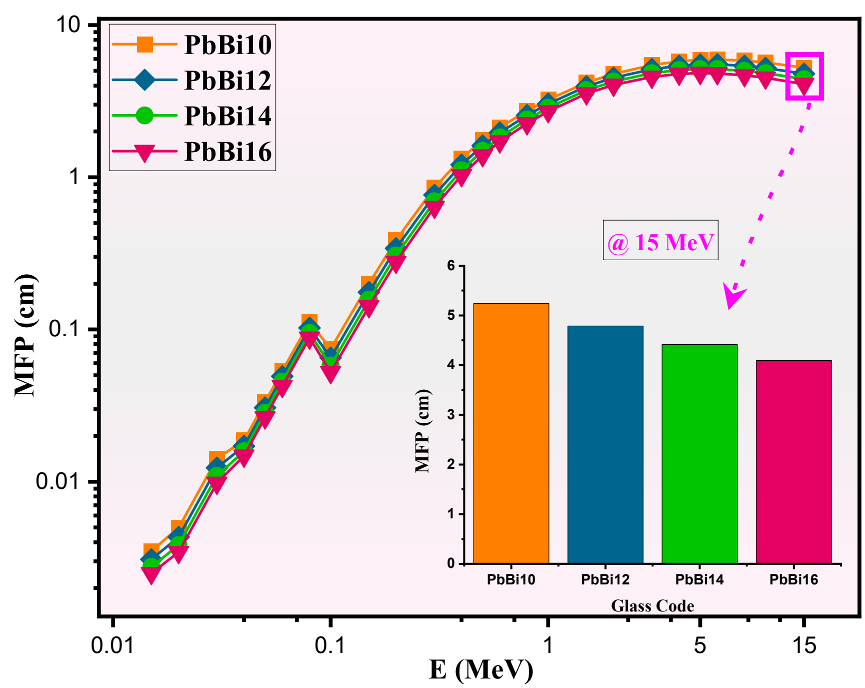

Figure 12: The MFP of the TeO_2-Bi_2O_3-PbO_2-B_2O_3 glasses.

The comparative analysis was performed against several previously reported glass matrices to determine the practical standing of the synthesized glass system among existing radiation shields. The chemical compositions and heavy-metal contents of these reference materials differ. The evaluation of the current glasses against glasses modified with WO_3, TeO_2, GeO_2, MoO_3, or SrO allows for a direct assessment of the competitiveness and suitability for advanced industrial and medical applications. Fig. 13a compares the MAC of the TeO_2-Bi_2O_3-PbO_2-B_2O_3 glasses with those reported for WO_3-MgO-B_2O_3-TeO_2-GeO_2 glasses [38]. PbBi16 and PbBi14 have higher MAC than all the WO_3-MgO-B_2O_3-TeO_2-GeO_2 glasses, since it contains relatively high amounts of Bi_2O_3 and PbO_2. PbBi12 has comparable MAC with 15WO_3-35MgO-20B_2O_3-20TeO_2-10GeO_2 glass. Fig. 13b compares the MAC of the TeO_2-Bi_2O_3-PbO_2-B_2O_3 glasses with those reported for SrO-B_2O_3-TeO_2 with different modifiers [39]. All the TeO_2-Bi_2O_3-PbO_2-B_2O_3 glasses have higher MAC than SrO-B_2O_3-TeO_2 glasses with V_2O_5, MnO_2, MoO_3 and TiO_2. Fig. 13c compares the MAC of the TeO_2–Bi_2O_3-PbO_2-B_2O_3 glasses with those reported for zinc boro tellurite glasses modified with PbO, Bi_2O_3 and MoO_3 [40]. PbBi16 has comparable MAC with 10ZnO-35B_2O_3-35TeO_2-20Bi_2O_3. The zinc boro tellurite glass modified with MoO_3 has lower MAC than all the TeO_2-Bi_2O_3-PbO_2-B_2O_3 glasses, while the zinc boro tellurite glass modified with PbO has comparable MAC with PbBi12.

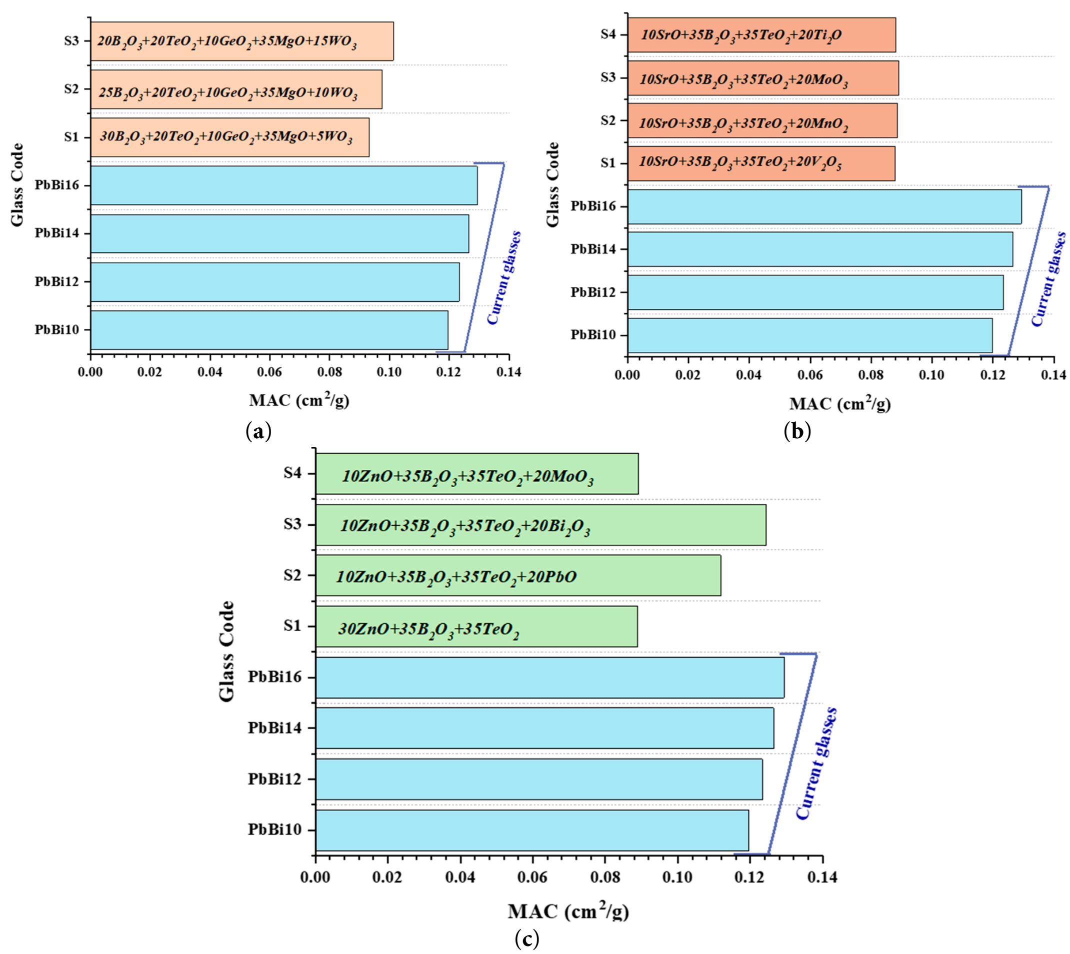

Figure 13: The MAC of the TeO_2-Bi_2O_3-PbO_2-B_2O_3 glasses in comparison with (**a**) B_2O_3-TeO_2-GeO_2-MgO-WO_3 glasses (**b**) SrO-B_2O_3-TeO_2 with different modifiers (**c**) zinc boro tellurite glasses modified with PbO, Bi_2O_3 and MoO_3.

4 Conclusion

The addition of PbO_2 and Bi_2O_3 results in an increase in density (4.759–5.561 g cm^{-3}) and molar volume (32.194–33.657 cm^3 mol^{-1}). The decrease in OPD (80.761–75.468 g-atom/L) confirmed expansion of the network rich in NBOs. The elastic moduli are in a decreasing trend. The E_g decreases from 2.969 eV to 2.813 eV. The n rises from 2.405 to 2.449. The metallization criterion decreased from 0.385 to 0.375. It indicates a shift toward semi-conducting behavior. Gamma-ray shielding evaluations using Phy-X software confirmed that the attenuation capacity significantly improved with the addition of HMOs. The high-density PbBi16 sample exhibited the highest MAC. The MAC reaches a maximum of 72.00 cm^2/g at 0.015 MeV as compared to 59.94 cm^2/g for the PbBi10 sample. Consequently, the PbBi16 glass provided the most space-efficient shielding, demonstrating the lowest HVL. It establishes that the PbBi16 glass is a highly effective material for advanced radiation protection applications.

Acknowledgement: The authors express their gratitude to the Princess Nourah bint Abdulrahman University, Riyadh, Saudi Arabia for its support.

Funding Statement: The authors express their gratitude to the Princess Nourah bint Abdulrahman University Researchers, Supporting Project Number (PNURSP2026R2), Princess Nourah bint Abdulrahman University, Riyadh, Saudi Arabia.

Author Contributions: Aljawhara H. Almuqrin—conceptualization, methodology, writing original draft, funding acquisition; Manjunatha—data curation, validation, investigation; M. I. Sayyed—supervision, writing original draft, formal analysis, visualization; Ashok Kumar—conceptualization, methodology, writing original draft, review & editing; A. S. Bennal—data curation, validation, investigation. All authors reviewed and approved the final version of the manuscript.

Availability of Data and Materials: The datasets generated during and/or analyzed during the current study are available from the corresponding author on reasonable request.

Ethics Approval: Not applicable.

Conflicts of Interest: The authors declare no conflicts of interest.

Supplementary Materials: The supplementary material is available online at https://www.techscience.com/doi/10.32604/cl.2026.083065/s1.

References

1. Chmielewski AG. Radiation technologies: the future is today. Radiat Phys Chem. 2023;213:111233. [CrossRef].
2. Zhan L, Bo Y, Lin T, Fan Z. Development and outlook of advanced nuclear energy technology. Energy Strategy Rev. 2021;34:100630. [CrossRef].
3. Mohan S, Chopra V. Chapter 18—biological effects of radiation. In: Radiation dosimetry phosphors. Cambridge, UK: Woodhead Publishing; 2022. p. 485–508. [CrossRef].
4. Wu Y, Wang Z. Progress in ionizing radiation shielding materials. Adv Eng Mater. 2024;26(21):2400855. [CrossRef].
5. Şensoy AT, Gökçe HS. Simulation and optimization of gamma-ray linear attenuation coefficients of barite concrete shields. Constr Build Mater. 2020;253:119218. [CrossRef].
6. Abdullah MAH, Rashid RSM, Amran M, Hejazii F, Azreen NM, Fediuk R, et al. Recent trends in advanced radiation shielding concrete for construction of facilities: Materials and properties. Polymers. 2022;14(14):2830. [CrossRef].
7. Solak BB, Aktas B, Yilmaz D, Kalecik S, Yalcin S, Acikgoz A, et al. Exploring the radiation shielding properties of B_2O_3-PbO-TeO_2-CeO_2-WO_3 glasses: a comprehensive study on structural, mechanical, gamma, and neutron attenuation characteristics. Mater Chem Phys. 2024;312:128672. [CrossRef].
8. Hafez S, Gomaa WM, Salama E. Optimizing gamma radiation shielding of low bismuth borate glass via antimony addition: optical and physical insights. Sci Rep. 2026;16(1):7511. [CrossRef].
9. Sayyed MI, Manjunatha, Bennal AS, Hanfi MY, Bhovi VK, Issa SAM. Impact of Y_2O_3 and Sm_2O_3 doping on the radiation shielding properties of lead-borate glasses. Appl Radiat Isot. 2026;229:112407. [CrossRef].

10. Mwakuna AE, Manepalli RKNR, Laxmikanth C. Structural, elastic and gamma-ray attenuation properties of potassium borate glasses doped with BaO, Bi_2O_3, or Pb_3O_4: a comparative assessment. Opt Mater. 2024;157:116294. [CrossRef].
11. Al-Buriahi MS, Alsaiari NS, Baskin MU, Olarinoye IO. Recent progress in the radiation shielding performance of common glass systems: the roles of different class of modifiers. J Radiat Res Appl Sci. 2025;18(1):101264. [CrossRef].
12. Mahraz ZAS, Sazali ES, Sahar MR. Spectral and dielectric characteristics of Er^{3+}-doped multicomponent tellurite glasses. Optik. 2021;239:166776. [CrossRef].
13. Ayuni JN, Halimah MK, Talib ZA, Sidek HA, Daud WM, Zaidan AW, et al. Optical properties of ternary TeO_2-B_2O_3-ZnO glass system. IOP Conf Ser Mater Sci Eng. 2011;17:012027. [CrossRef].
14. Hegazy HH, Al-Buriahi MS, Alresheedi F, El-Agawany FI, Sriwunkum C, Neffati R, et al. Nuclear shielding properties of B_2O_3-Bi_2O_3-SrO glasses modified with Nd_2O_3: theoretical and simulation studies. Ceram Int. 2021;47(2):2772–80. [CrossRef].
15. Zakaly HMH, Issa SAM, Saudi HA, Soliman TS. Decoding the role of bismuth oxide in advancing structural, thermal, and nuclear properties of [B_2O_3-Li_2O-SiO_2]-Nb_2O_5 glass systems. Radiat Phys Chem. 2024;223:111984. [CrossRef].
16. Rammah YS, Mahmoud KA, Kavaz E, Kumar A, El-Agawany FI. The role of PbO/Bi_2O_3 insertion on the shielding characteristics of novel borate glasses. Ceram Int. 2020;46(15):23357–68. [CrossRef].
17. Ahammed S, Srinivas B, Shareefuddin M. Role of potassium fluoride on CdO-59B_2O_3-CuO glasses: a physical and structural study. Eur Phys J Plus. 2025;140(12):1269. [CrossRef].
18. Srinivas B, Bhemarajam J, Bhogi A, Prasad PS, Shareefuddin M. Highly efficient and stable Cr^{3+} activated SrO-TeO_2-TiO_2-B_2O_3 glasses for LED applications. Ceram Int. 2025;51(17):23077–89. [CrossRef].
19. Galhoum AA, Abou-Krisha MM, Alsulami SR, El-Seidy AMA. Build-up shielding-factors, physical, and structural properties of $CuBi_2O_4$/PVA nanocomposite films. J Alloys Compd. 2026;1068:188447. [CrossRef].
20. Abo-Mosallam HA, Abdelglil MI, Bayoumi EE, El-Seidy AMA. Build-up shielding-factors, physical & mechanical properties of Er^{3+} doped borophosphate glasses with varied Bi_2O_3 content. RSC Adv. 2026;16(15):13007–20. [CrossRef].
21. Pisarski WA, Pisarska J, Ryba-Romanowski W. Structural role of rare earth ions in lead borate glasses evidenced by infrared spectroscopy: $BO_3 \leftrightarrow BO_4$ conversion. J Mol Struct. 2005;744–7:515–20.[CrossRef].
22. Saritha D, Markandeya Y, Salagram M, Vithal M, Singh AK, Bhikshamaiah G. Effect of Bi_2O_3 on physical, optical and structural studies of ZnO–Bi_2O_3–B_2O_3 glasses. J Non Cryst Solids. 2008;354(52):5573–9. [CrossRef].
23. Singh GP, Singh J, Kaur P, Kaur S, Arora D, Kaur R, et al. Comparison of structural, physical and optical properties of Na_2O-B_2O_3 and Li_2O-B_2O_3 glasses to find an advantageous host for CeO_2 based optical and photonic applications. J Non Cryst Solids. 2020;546:120268. [CrossRef].
24. Bashir AR, Rana AM, Ullah S, Shah SIW, Wazir-ud-Din M. Investigation of the radiation shielding and physical properties of strontium-zinc-borate glasses. Nexus Futur Mater. 2025;2:245. [CrossRef].
25. Gaikwad KB, Gattu KP, More CV, Pawar PP. Physical, structural and nuclear radiation shielding behavior of Ni–Cu–Zn Fe_2O_4 ferrite nanoparticles. Appl Radiat Isot. 2024;207:111244. [CrossRef].
26. Effendy N, Zaid MHM, Matori KA, Iskandar SM, Hisam R, Azlan MN, et al. Fabrication of novel BaO–Al_2O_3–Bi_2O_3–B_2O_3 glass system: Comprehensive study on elastic, mechanical and shielding properties. Prog Nucl Energy. 2022;153:104418. [CrossRef].
27. Alazoumi SH, Sidek HAA, Halimah MK, Matori KA, Zaid MHM, Abdulbaset AA. Synthesis and elastic properties of ternary ZnO-PbO-TeO_2 glasses. Chalcogenide Lett. 2017;14(8):303–20.
28. Abul-Magd AA, Abu-Khadra AS, Abdel-Ghany AM. Influence of La_2O_3 on the structural, mechanical and optical features of cobalt doped heavy metal borate glasses. Ceram Int. 2021;47(14):19886–94. [CrossRef].
29. Makishima A, MacKenzie JD. Direct calculation of Young's moidulus of glass. J Non Cryst Solids. 1973;12(1):35–45. [CrossRef].
30. Makishima A, MacKenzie JD. Calculation of bulk modulus, shear modulus and Poisson's ratio of glass. J Non Cryst Solids. 1975;17(2):147–57. [CrossRef].
31. Inaba S, Oda S, Morinaga K. Heat capacity of oxide glasses at high temperature region. J Non Cryst Solids. 2003;325(1–3):258–66. [CrossRef].

32. Sallam OI, Rammah YS, Nabil IM, El-Seidy AMA. Enhanced optical and structural traits of irradiated lead borate glasses via Ce^{3+} and Dy^{3+} ions with studying Radiation shielding performance. Sci Rep. 2024;14(1):24478. [CrossRef].
33. Rayan DA, Elbashar YH, Rashad MM, El-Korashy A. Optical spectroscopic analysis of cupric oxide doped barium phosphate glass for bandpass absorption filter. J Non Cryst Solids. 2013;382:52–6. [CrossRef].
34. Şakar E, Özpolat ÖF, Alım B, Sayyed MI, Kurudirek M. Phy-X/PSD: Development of a user friendly online software for calculation of parameters relevant to radiation shielding and dosimetry. Radiat Phys Chem. 2020;166:108496. [CrossRef].
35. Gaber EA, Hussien SA, Saad EM, Mahmoud AE. Effect of Bi^{3+} on the structural, optical and simulate γ-radiation shielding features of borate glasses doped nickel ions. Radiat Phys Chem. 2024;218:111579. [CrossRef].
36. Sanghi S, Pal I, Agarwal A, Aggarwal MP. Effect of Bi_2O_3 on spectroscopic and structural properties of Er^{3+} doped cadmium bismuth borate glasses. Spectrochim Acta Part A Mol Biomol Spectrosc. 2011;83(1):94–9. [CrossRef].
37. Iliyasu U, Mohd Sanusi MS, Ahmad NE, Al-Buriahi MS, Thabit HA, Sifawa AA. Impact of Bi_2O_3 on the optical, structural, thermal, and nuclear radiation shielding properties of lead zinc borate glass. Phys B Condens Matter. 2025;705:417076. [CrossRef].
38. Hamad MK. Effect of WO_3 on structural, optical, mechanical, and ionizing radiation shielding properties of borate-tellurite glass network. Ceram Int. 2025;51(8):9763–71. [CrossRef].
39. Sayyed MI, Hamad MK, Mhareb MHA, Prabhu NS, Khosravi H, Kamath SD. Effect of different modifiers on mechanical and radiation shielding properties of SrO-B_2O_3-TeO_2 glass system. Optik. 2022;257:168823. [CrossRef].
40. Mhareb MHA, Sayyed MI, Mekki A, Dwaikat N, Alshamari A, Hamad MK, et al. Radiation shielding features and X-ray photoelectron spectroscopy for zinc boro tellurite glasses modified with various oxides. Radiat Phys Chem. 2025;237:113127. [CrossRef].